Structures, Phase Fields and Mixed Protonic-Electronic Conductivity of Ba-deficient, Pr-substituted $BaZr_{0.7}Ce_{0.2}Y_{0.1}O_{3-\delta}$

Gemma Heras-Juaristi[a], Ulises Amador[b], Julio Romero de Paz[c], Rodolfo O. Fuentes[d], Adilson L. Chinelatto[e], Clemens Ritter[f], Duncan P. Fagg[g]

Domingo Pérez-Coll[a], Glenn C. Mather[a*]

[a]*Instituto de Cerámica y Vidrio, CSIC, Cantoblanco, 28049 Madrid, Spain*

[b]*Quimica Facultad de Farmacia, Universidad CEU-San Pablo, Boadilla del Monte, Madrid 28668, Spain*

[c]*C.A.I. Técnicas Físicas, Facultad de Ciencias Físicas, Universidad Complutense, 28040 Madrid, Spain*

[d]*Dept. de Física de la Materia Condensada, CNEA, Av. Gral. Paz 1499, 1650 Buenos Aires, Argentina*

[e]*Dept. de Engenharia de Materiais, Universidade Estadual de Ponta Grossa, Av. Gal. Carlos Cavalcanti, 4748, 84030-900- Ponta Grossa-PR, Brazil*

[f]*Institut Laue-Langevin, 71 Avenue des Martyrs, Grenoble 38042, France*

[g]*Department of Mechanical Engineering, University of Aveiro, 3810-193 Aveiro, Portugal*

*mather@icv.csic.es; Tel. 0034 917355840.

Abstract

The $BaZr_{0.7}Ce_{0.2}Y_{0.1}O_{3-\delta}$-$BaPrO_{3-\delta}$ perovskite system, of interest for high-temperature electrochemical applications involving mixed protonic-electronic conductivity, forms a solid solution with a wide interval of Ba substoichiometry in the range $Ba(Ce_{0.2}Zr_{0.7})_{1-x}Pr_xY_{0.1}O_{3-\delta}$, $0 \leq x \leq 1$. Structural phase transitions mapped as a function of temperature and composition by high-resolution neutron powder diffraction and synchrotron X-ray diffraction reveal higher symmetry for lower Pr content and higher temperatures, with the largest stability field observed for rhombohedral symmetry (space group, $R\bar{3}c$). Rietveld refinement, supported by magnetic-susceptibility measurements, indicates that partitioning of the B-site cations over the A and B perovskite sites compensates Ba substoichiometry in preference to A-site vacancy formation and that multiple cations are distributed over both sites. Electron-hole transport dominates electrical conductivity in both wet and dry oxidising conditions, with total conductivity reaching a value of ~ 0.5 $S.cm^{-1}$ for the x = 1 end-member in dry air at 1173 K. Higher electrical conductivity and the displacement of oxygen loss to higher temperatures with increasing Pr content both reflect the role of Pr in promoting hole formation at the expense of oxygen vacancies. In more reducing conditions (N_2) and at low Pr contents, conductivity is higher in humidified atmospheres (~ 0.023 atm pH_2O) indicating a protonic contribution to transport, whereas the greater electron-hole conductivity with increasing Pr content results in lower conductivity in humidified N_2 due to the creation of protonic defects and the consumption of holes.

Introduction

The development of mixed-conducting protonic-electronic ceramic materials is of considerable interest for a number of high-temperature electrochemical applications involving hydrogen. Barium cerium-zirconate solid solutions with the perovskite (ABO_3) structure have emerged as strong candidate materials for electrochemical membranes, with much focus on the composition $BaZr_{0.7}Ce_{0.2}Y_{0.1}O_{3-\delta}$ (BZCY72)[1,2], which provides both good stability and moderately high proton transport [3].

The conversion of hydrogen to electrical energy may take place in protonic ceramic fuel cells (PCFCs) which operate within an intermediate temperature range (773 -973 K) employing BZCY72 or related solid-solution members as electrolytes. Lower temperatures are more advantageous for long-term stability, balance-of-plant costs and miniaturization; however, with lower temperature, large overpotentials are encountered at the electrode-electrolyte interface due to slower reaction kinetics. The role of the cathode is, therefore, crucial to fuel efficiency in this temperature range. The influence of proton and oxide-ion conductivities on cathode performance in PCFCs has not been clearly established. Although different electrode designs have been experimented, it is nevertheless apparent that high electron (or electron hole) transport is essential.

One strategy to improve cathode performance is through the introduction of greater electronic conductivity in a proton-conducting phase. For example, Fabbri et.al. induced higher electronic transport in $BaZr_{0.9}Y_{0.1}O_{3-\delta}$ on substituting Zr by Pr [4] but the conductivity was still too low for application as a single-phase cathode. In contrast, the approach of substituting electronically-conducting perovskite SOFC cathode compositions with cations that may induce proton transport, in particular Zr-doped

$Ba(Co,Fe,Y)O_{3-\delta}$ [5,6], has led to very low polarization resistances for both PCFCs and oxide-ion-based solid oxide fuel cells (SOFCs). Similarly, mixed protonic-electronic conduction is required in membrane technologies for hydrogen separation, which may be coupled with useful reactions such as the reduction of CO_2[7] or methane dehydroaromatization [8], whereby natural gas is converted in a non-oxidative process to aromatics.

Praseodymium is an interesting dopant for perovskite cerates and zirconates as it can, in principle, occupy both A and B sites[9], increase sinterability[10] and augment electronic conductivity[11,12]. Although compositions with low levels of Pr doping are reported to exhibit good stability[10], Pr-rich perovskites are associated with poor stability in wet and reducing gases[12–14]. We have recently studied the effects of Pr substitution in BZCY72, finding that substitution of Zr/Ce with Pr led to higher electronic conductivity and a number of symmetry changes dependent on Pr content and temperature[15]. Of interest in this and other recent related studies of the Pr-substituted $BaZrO_3$ system [9,16] was the finding that Pr resides exclusively on the perovskite B site in the IV oxidation state, despite the fact that ion site-size requirements indicate Pr^{3+} is much more likely to occupy the A site. Mixed Pr oxidation states were, therefore, discounted as the origin of the enhanced thermally activated electronic conductivity. It was also reported that the type of charge-compensation mechanism for Pr substitution is highly dependent on the Pr concentration.

In general, A-site deficiency is a widely adopted strategy for tailoring the defect chemistry and doping mechanisms in technologically relevant perovskites in order to improve the physicochemical properties[17–20]. A-site substoichiometry in Y-doped $BaZrO_{3-\delta}$ (BZY) arising from Ba evaporation on sintering is considered to be compensated

by partitioning of the Y dopant on the A site leading to a decrease in proton conductivity and unit cell constant[21]. On the other hand, Ba deficiency in $BaCeO_3$-based phase was recently reported to lower grain-boundary resistances and improve stability by cleaning the grain boundaries of an amorphous nanometer-thick barium oxide layer[22]. The effects on electrical properties and defect chemistry of engineering compositions with potential for either A-site vacancy formation or dopant partitioning in Pr-doped systems have been studied for a limited range of A-site nonstoichiometry in the case of $Ba_{0.95}Zr_{0.8}Pr_{0.2}O_{3-\delta}$, revealing redistribution of Pr over both A and B sites and partial reduction of Pr^{4+} to Pr^{3+}, especially at high temperatures in reducing conditions [9]. The combined effects of A-site deficiency and dopant partitioning often occur unintentionally as a result of high-temperature firing but may also be extremely useful for engineering transport, stability and electrocatalytic properties.

In this paper, continuing our exploration of the BZCY72-$BaPrO_3$ system with potential application as mixed protonic, oxide-ionic and electronic conductors for high-temperature electrochemical devices, we report the synthesis of the solid solution $Ba(Zr_{0.7}Ce_{0.2})_{1-x}Pr_xY_{0.1}O_{3-\delta}$ in which Ba substoichiometry increases with x. We map the structural phase transitions occurring in the $Ba(Zr_{0.7}Ce_{0.2})_{1-x}Pr_xY_{0.1}O_{3-\delta}$ system as a function of temperature and composition by high-resolution neutron powder diffraction supplemented by synchrotron radiation X-ray diffraction (SR-XRD) in different atmospheres. The structural information, complemented by magnetic-susceptibility measurements to assess the Pr oxidation state and the consequent Pr-site distribution, is employed to analyse the effects of Ba substoichiometry and Pr substitution on electrical conductivity, determined in dry and humidified air and N_2 atmosphere by impedance spectroscopy.

Experimental

Members of the solid-solution series $Ba(Zr_{0.7}Ce_{0.2})_{1-x}Pr_xY_{0.1}O_{3-\delta}$ (x = 0, 0.2, 0.4, 0.6, 0.8, 1.0) were synthesized by a citrate-nitrate process based on the Pechini method. The water content of the nitrate precursors was firstly determined by thermogravimetry in air with an SDT Q600 instrument. The appropriate stoichiometric ratio of nitrates was added to deionised water heated at 323 K on a hotplate in the order $Ba(NO_3)_2.xH_2O$, $ZrO(NO_3)_2.xH_2O$, $Ce(NO_3)_3.xH_2O$, $Y(NO_3)_3.xH_2O$ and $Pr(NO_3)_3.xH_2O$. On obtaining a transparent green solution, the temperature was first raised in the range 333-353 K for ~ 2 hours then subsequently to > 363 K for 4-5 hours, and finally to above 373 K for over 12 hours. The obtained dark-brown polymerized complex was then pyrolysed in an oven at 623 K for 4 h. The resulting polymeric precursor was heated at 873 K for 4 h, milled and heat treated at 1373 K for a further 4 h to remove any remaining organic product, before attrition milling in Teflon vials and sieving (100 μm). Phase analysis and structural characterisation were performed on powders prepared by uniaxially pressing the as-prepared powder into 10 mm-diameter cylindrical pellets, covering with sacrificial powder of the same composition and firing in the range 1623-1773 K for 4 hours. The pellets were then crushed and milled in an agate mortar and pestle in acetone. Pellets were prepared for electrochemical and magnetic measurements after treatment at 1373 K employing a further heat treatment at 1523 K for 24 h with intermediate grinding followed by attrition milling and sieving (100 μm) prior to sintering the pressed powders at 1923 K for 4-8 h.

Phase analysis was initially performed by powder X-ray diffraction (XRD) on a Bruker D8 high-resolution diffractometer, using monochromatic Cu $K\alpha_1$ radiation (λ =

1.5406 Å). Neutron powder diffraction (NPD) measurements were conducted on the high-resolution D2B diffractometer at the Institut Laue Langevin (Grenoble, France) on heating within a temperature range of 299 – 1173 K. A Ge monochromator was employed to select a monochromatic beam wavelength of 1.594 Å from the primary beam. Synchrotron radiation X-ray diffraction (SR-XRD) patterns were recorded on samples mounted on a ceramic sample holder and heated in a furnace in the range 500 - 900°C in controlled atmospheres of dry and wet synthetic air (flow rate, 50 ml.min^{-1}) and dry N_2 (100 ml.min^{-1}) at the D10B-XPD beamline of the National Synchrotron Light Laboratory (LNLS, Campinas, Brazil). The X-ray wavelength was set to 1.54915 Å. Data in the range $20 \leq 2\theta \leq 90°$ were collected in step-scanning mode, with a step length of 0.005° and a step-counting time of 2 s. Samples were heated at a rate of 10 °C.min^{-1}, and a dwell time of 10 min was employed at each temperature before performing the XRD scan. NIST SRM 640c Si powder was used as the standard for the instrumental broadening correction. Structural refinements of the NPD and SR-XRD data were performed by the Rietveld method with the Fullprof program[23].

The temperature dependence of the molar magnetic susceptibility χ of the series was determined with a superconducting quantum interference device magnetometer (Quantum Design, model MPMS-XL). Polycrystalline samples were measured according to the procedure described elsewhere [15].

Thermogravimetric analysis (TGA) was performed with an initial heating-cooling cycle in synthetic air on heating at 10 K·min^{-1} in the temperature range 298 – 1303 K followed by a further heating cycle in 100 % CO_2 with a heating rate of 5 K·min^{-1} to check stability versus the formation of $BaCO_3$.

Cylindrical pellets were prepared for electrical measurements by coating the faces with Heraeus Pt paste (CL11-5349) and firing at 1173 K for 1 hour. Impedance spectroscopy was employed to determine conductivity as a function of temperature on cooling in steps of 50 K in the temperature range 423 – 1173 K employing an Autolab PGStat302N instrument operating over the frequency range $0.1 \leq f \leq 10^6$ Hz with a signal amplitude of 50 mV in potentiostatic mode. Measurements were registered in dry atmospheres of air and N_2 on feeding the gas directly through a drying column containing a commercial moisture trap of aluminosilicate- and zeolite-based beads. For wet air and N_2 atmospheres, the gas was firstly bubbled through KBr-saturated water at room temperature to provide a water content of ~ 0.023 atm. Analysis of impedance spectra was performed with the Zview 2.9c software (Scribner Associates) by fitting the data to appropriate equivalent circuits in order to resolve the impedance response into bulk, grain-boundary and electrode contributions.

Results and Discussion

Phase Formation, Phase Fields and Cation Distribution

Solid-solution formation was confirmed by XRD for the complete $Ba(Zr_{0.7}Ce_{0.2})_{1-x}Pr_xY_{0.1}O_{3-\delta}$ series on sintering at 1698 K for 4 h; the nominal compositions of the series are listed in Table 1 (column 1). Peak splitting for the series enhanced with increasing Pr content indicating more complex structural detail associated with octahedral tilting. High-resolution neutron powder diffraction is most useful in the analysis of the concerted oxygen movements in these tilted perovskites and, in turn, for the precise determination of space group due to the much higher neutron scattering factor of

oxygen in comparison to that of X-rays, as has been recently demonstrated for BZCY72 [24] and the related Ba stoichiometric solid solution [15].

Superlattice reflections in the NPD patterns confirmed that the title series was distorted from the cubic perovskite aristotype and were indexed in accordance with the method of Glazer [25] and Woodward and Reaney [26]. The ½{o o o} pattern (where "o" represents an odd-number index) of the simple cubic unit cell observed for both the present and sister series[27] is compatible with uniquely antiphase tilting of the BO_6 octahedra, with possible space groups *I4/mcm*, *Imma* and $R\bar{3}c$. The final symmetry was determined through analysis of the superlattice reflections originating from the distortion of the aristotype and inspection of the corresponding refinement quality criteria.

The NPD data were fitted in the temperature range RT- 333K using the appropriate orthorhombic, rhombohedral or cubic structural model with both an A-site-vacancy mechanism (Kröger-Vink notation):

$$Ba_{Ba}^{\times} + O_O^{\times} \rightarrow V_{Ba}^{//} + V_O^{\cdot\cdot} + BaO \qquad (1)$$

and a partition mechanism involving distribution of the B-site species over both A and B sites[20], expressed below for the case of Pr:

$$2Ba_{Ba}^{\times} + 2O_O^{\times} + Pr_B^{/} + V_O^{\cdot\cdot} \rightarrow Pr_{Ba}^{\cdot} + 2BaO \qquad (2)$$

$$\left(V_{Ba}^{//} + V_B^{////} + 3V_O^{\cdot\cdot} \rightarrow null\right)$$

Note that this mechanism is preceded by the formation of a Pr^{3+} species

$$2Pr_B^{\times} + O_O^{\times} \rightarrow 2Pr_B^{/} + V_O^{\cdot\cdot} + \frac{1}{2}O_2 \qquad (3)$$

Although, reduction creates oxygen vacancies, the overall dopant partitioning mechanism (eqs. (2) and (3)) leads to consumption of oxygen vacancies whereas they are created *via* the A-site vacancy mechanism (1). Further compensation regimes, such as occupation of the A site by a B-site cation and concomitant formation of either B-site cation vacancies or oxygen interstitials, were discounted based on their expected improbably high energy penalties. Cation ordering on either cation site was also disregarded due to the absence of associated supercell reflections. The refinement quality criteria on refining according to either the A-site vacancy or partition mechanism with the compositions indicated in Table 1 (columns 2 and 3) generally improved for the latter, indicating full A-site occupancy; the percentage improvement of R_{Bragg} and χ^2 employing the partition mechanism over the vacancy mechanism is shown in Fig. 1.

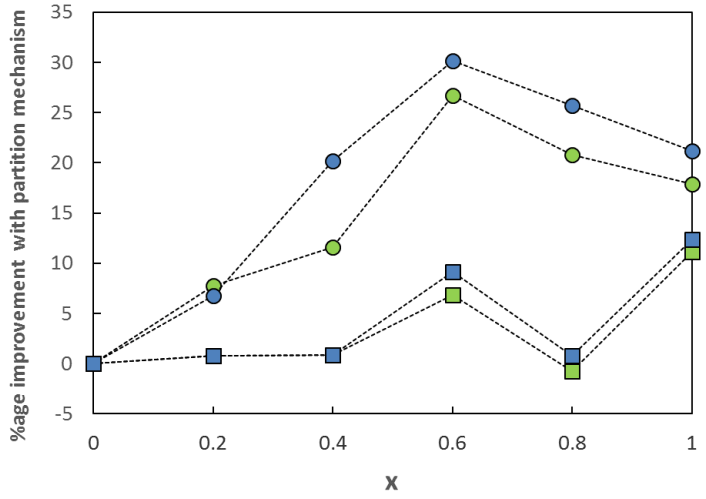

Fig. 1. Percentage improvement of the Rietveld refinement criteria R_{Bragg} $\left(\left(\frac{R_{B,vac}-R_{B,part}}{R_{B,vac}}\right)*100\%\right)$, shown as circles, and χ^2 $\left(\left(\frac{\chi^2_{vac}-\chi^2_{part}}{\chi^2_{vac}}\right)*100\%\right)$, shown as squares, of the $Ba(Zr_{0.7}Ce_{0.2})_{1-x}Pr_xY_{0.1}O_{3-\delta}$ series on employing the partition mechanism of charge compensation with only Pr (green) and with a multiple-cation partition

mechanism (blue), according to Table 1, in comparison to the vacancy mechanism. Data were determined from ND at 573 K.

In order to clarify the oxidation state and site distribution of the paramagnetic praseodymium atoms in the $Ba(Zr_{0.7}Ce_{0.2})_{1-x}Pr_xY_{0.1}O_{3-\delta}$ series, we compared the magnetism of the Pr-rich end member (x = 1) with that of nominally Ba stoichiometric $BaPr_{0.9}Y_{0.1}O_{3-\delta}$[15]. Note that both phases have similar nominal composition with respect to the B-site cations. It is well known that the theoretical value for a free Pr^{4+} cation in its J = $\frac{5}{2}$ ground state, 2.54 μ_B, is largely reduced when it is located in an octahedral site, such as the B-site of the perovskite–type structure; reduced magnetic-moment values usually range from 0.68 μ_B for $BaPrO_3$ [28] to 1.57 μ_B for $SrPrO_3$ [29]. The rather low magnetic moment value (0.65 $\pm$ 0.02 μ_B) determined for the paramagnetic praseodymium ion of $BaPr_{0.9}Y_{0.1}O_{3-\delta}$ strongly supported a B-site location and +4 oxidation state for Pr in this case[15]. Further evidence for this was the weak ferromagnetism observed below 9.5 K due to long-range antiferromagnetic ordering of Pr^{4+} moments, as in the case of $BaPrO_3$ oxide with a Néel temperature of T_N =11.6 K [30,31]; the partial substitution of praseodymium by yttrium accounts for the slightly different ordering temperatures between the two phases.

The temperature dependence of the magnetic susceptibility χ obtained for the x = 1 member of the current series is shown in Fig. 2. The increase of χ as temperature decreases from room temperature down to 30 K corresponds to paramagnetic behaviour well described by the modified Curie-Weiss law $\chi = \frac{C}{T-\theta} + \chi_0$, where the Curie constant (C), the Weiss temperature (θ) and the temperature-independent paramagnetism (χ_0) take the values $1.059\times10^{-1} \pm 2\times10^{-4}$ emu K mol Pr^{-1} Oe^{-1}, - 21.1 $\pm$

0.1 K and $6.228\times10^{-4} \pm 5\times10^{-7}$ emu mol Pr^{-1} Oe^{-1}, respectively.

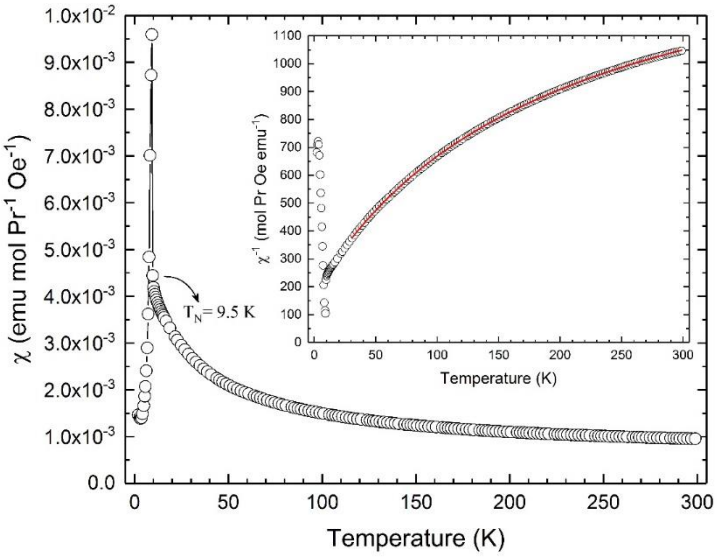

Fig. 2. Thermal variation of the magnetic susceptibility for member x = 1 of the $Ba(Zr_{0.7}Ce_{0.2})_{1-x}Pr_xY_{0.1}O_{3-\delta}$ series in an applied field of 100 mT. The solid black line is a guide for the eye. The inset shows the corresponding inverse magnetic susceptibility versus temperature plot and the solid red line is the best fit (r^2= 0.99999) of the data obtained between 30 and 300 K to the χ^{-1}function where $\chi = \frac{C}{T-\theta} + \chi_0$.

The sharp increase of χ observed at 9.5 K indicates an antiferromagnetic transition with a weak ferromagnetic component, analogous to that occurring in $BaPrO_3$ [30,31]. The magnetic moment calculated from the C value ($\mu = \sqrt{8C}$) is 0.92 $\pm$ 0.01 μ_B, which is significantly larger than our reference value of 0.65 μ_B determined for $BaPr_{0.9}Y_{0.1}O_{3-\delta}$[15]. In contrast, both this phase and the x = 1 member of the present series exhibit an identical ordering temperature (T_N = 9.5 K), indicating that both the composition of the B sublattices and the effect of crystal field on Pr^{4+} must be very similar in both instances [32–34]. In light of this scenario, and consideration of ion site–size requirements, it follows that the presence of Pr^{3+} atoms on the perovskite A site accounts for the increment of the magnetic moment in the title series, assuming that the magnetic interactions involving Pr on the B site remain unchanged. The magnetic data strongly support,

therefore, the conclusions of the Rietveld refinement analysis that partitioning of Pr over the A and B perovskite sites compensates, at least in part, barium substoichiometry.

Nevertheless, the experimental magnetic moment for the x = 1 end member was found to be slightly lower than the theoretical value for a scenario with full Pr partitioning (Table 1, column 3) and, therefore, the full A-site occupancy must imply not only that Pr partially occupies the A site but that diamagnetic Y^{3+} cations are also distributed over both sites. The Rietveld refinements were repeated based on a multiple-cation partitioning (Table 1, column 4), leading to further improvement in the refinement quality criteria (blue symbols, Fig. 1.). Cerium partitioning over the A and B perovskite sites was discounted based on the higher energy required for the reduction of Ce^{4+} to Ce^{3+} as contrasted with the reduction of Pr^{4+} to Pr^{3+} [35]

There is, in general, a greater difference observed for the Bragg R-factor between the vacancy mechanism and the two partition mechanisms (Table 1) for later members of the series by NPD in Fig. 1 due to the greater sensitivity of this technique to site occupancies and the greater difference in site occupancies with increasing Pr content. We note that in other A-site deficient series, anomalous variations in unit-cell parameters with compositions are observed[36]. In the case of $Sr_{1-x}Ce_{0.9}Yb_{0.1}O_{3-\delta}$, this was attributed to a change in compensation mechanism for A-site vacancy to dopant partitioning with increasing A-site cation deficiency[20]. In the present study, Vegard's law is observed with lattice parameter vs x plots (not shown) exhibiting a high degree of linearity, suggesting that the compensation mechanism is unchanged throughout the series. Refinements were improved on employment of anisotropic temperature factors.

Final structural parameters of selected phases at low temperatures (RT- 333 K) are listed in Table 2. The corresponding observed and calculated NPD patterns are shown in Fig. 3.

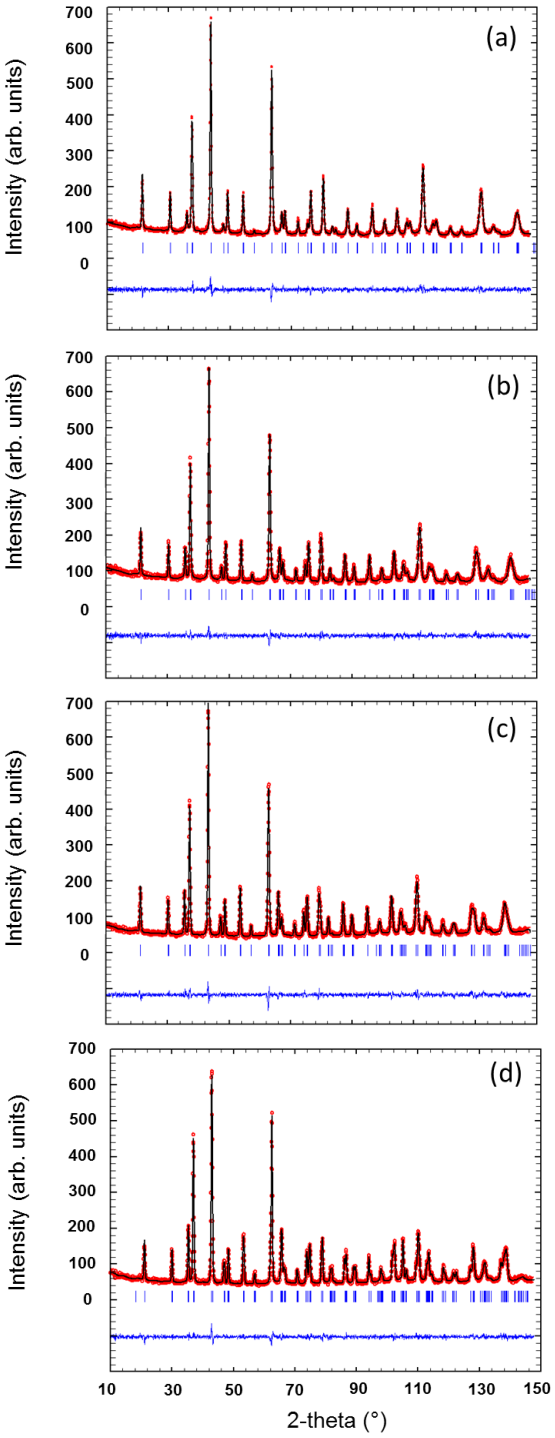

Fig. 3. Experimental (circles), calculated (continuous line) and difference (continuous line at bottom of each panel) neutron diffraction patterns for x= 0.2 (T = 40 °C) , 0.4 (RT), 0.6 (65 °C) and 0.8 (65 °C); the positions of Bragg peaks are indicated by vertical bars.

The phase fields of the series as a function of temperature and composition (x) as determined from the NPD data, Fig. 4., reflect the increasing tilting of the BO_6 octahedra with increasing x and lower temperature.

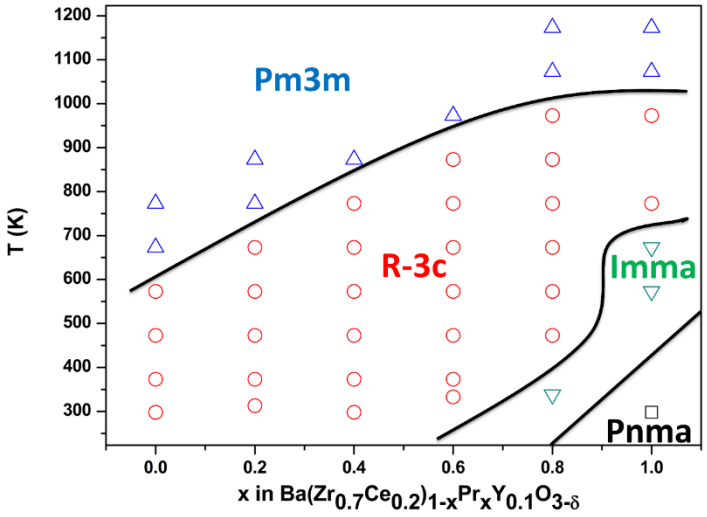

Fig. 4. Phase fields of the $Ba(Zr_{0.7}Ce_{0.2})_{1-x}Pr_xY_{0.1}O_{3-\delta}$ series determined from NPD data.

With greater Pr content, the Goldschmidt tolerance factor is lower due to the presence of the larger Pr^{4+} cation on the B site in comparison to the average ionic radii of the substituted Zr/Ce cations. The presence of the smaller B-site cations in comparison to Ba on the A site will also lower the tolerance factor. The stress associated with mismatch of the A-O and B-O bond lengths is partially alleviated with increasing temperature leading to higher symmetry structures. The transition to cubic symmetry which is displaced to higher temperature with increasing Pr content may be followed by the octahedral tilt angle (ϕ) calculated from the refined oxygen position of the hexagonal cell [37] and shown in Fig. 5 for x = 0.8.

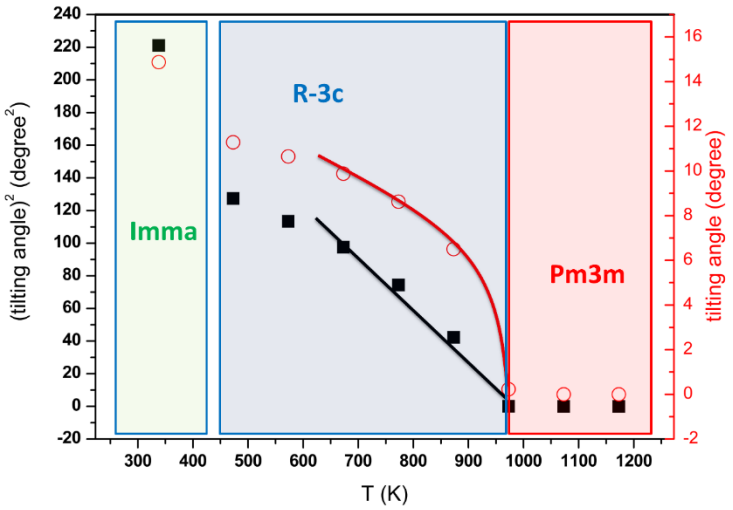

Fig. 5. The square of the octahedral tilt angle (ϕ) of the x = 0.8 member of the $Ba(Zr_{0.7}Ce_{0.2})_{1-x}Pr_xY_{0.1}O_{3-\delta}$ series as a function of temperature (squares, primary y-axis) and ϕ as a function of temperature (circles, secondary y-axis).

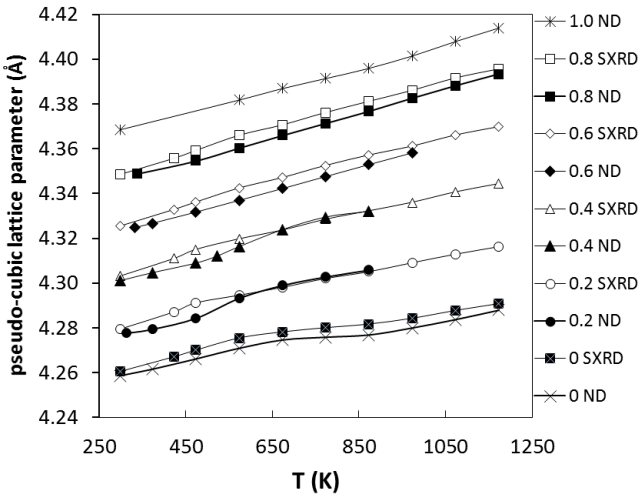

Fig. 6. Pseudo-cubic lattice constants of the $Ba(Zr_{0.7}Ce_{0.2})_{1-x}Pr_xY_{0.1}O_{3-\delta}$ series determined from ND data on heating in low vacuum or from SR-XRD data on heating in synthetic air.

The pseudo-cubic lattice parameters of the title series in the range RT – 1173 K determined from both NPD and SR-XRD data are shown in Fig. 6. The behaviour in air (SR-XRD data) is similar to that of the BZCY72 end-member[24] and the recently studied Ba-stoichiometric series[15], with a greater expansion in the low-temperature range followed by a return to purely thermal expansion observed for the Pr-lean series

members as temperature increases. This non-linearity was attributed to loss of water present in the as-prepared materials, and is observed for similar proton-conducting perovskites[38,39]. Analogous to the Ba stoichiometric series, later members exhibit greater linearity of lattice parameter with temperature, although deviations occur on undergoing a first-order phase transition from orthorhombic to rhombohedral symmetry. However, data for the Pr-containing members x = 0.2 and 0.4 collected in low vacuum (ND) deviate somewhat from this previously observed behaviour in that, in the range where the deviation from the expected thermal-expansion trend is most pronounced, the lattice parameter is lower then converges with the expected thermal expansion as temperature increases. It is speculated that this hitherto unobserved behaviour may be related to the different Pr site occupancy and valence states under low vacuum which differ to those observed in air or for the Ba stoichiometric series. The refined oxygen occupancy of the BZCY72 end-member phase decreased with increasing temperature, closely following the dehydration event[40]. In the present series, oxygen loss is also observed with increasing temperature, although the temperature at which the loss initiates is displaced to higher temperature with increasing Pr content, Fig. 7.

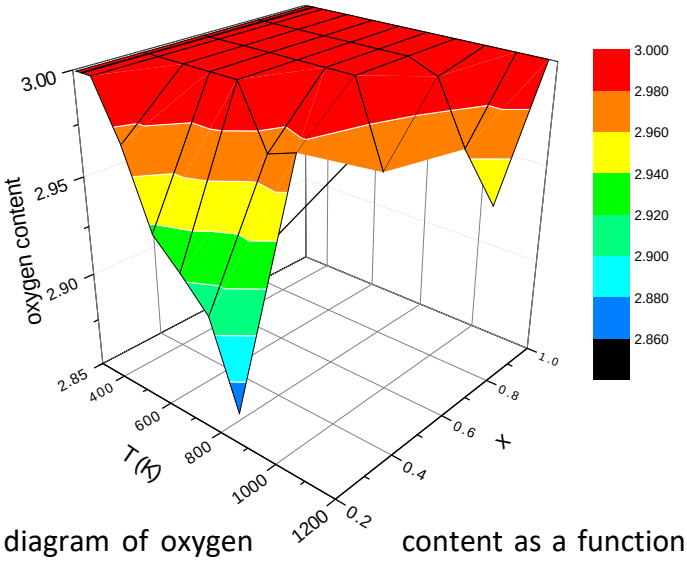

Fig. 7. Schematic diagram of oxygen content as a function of temperature and Pr content (x) for the $Ba(Zr_{0.7}Ce_{0.2})_{1-x}Pr_xY_{0.1}O_{3-\delta}$ series.

Relatedly, lattice parameters collected in N_2 in the range 500-900 °C with SR-XRD were slightly larger than those collected in wet or dry air (not shown), most probably resulting from a small amount of reduction associated with oxygen loss. This behaviour is discussed more fully in the context of interpretation of the electrical-conductivity data.

Thermal behaviour in CO_2

Thermogravimetry was performed on heating in CO_2 to provide a preliminary comparison of stability within the series. Samples were firstly heated to 1173 K and cooled in synthetic air prior to heating in CO_2. The change in mass during the air cycle varied within a narrow range and did not provide a reliable indication of water content. Significant mass loss which could be attributed to reduction of Pr^{4+} or Ce^{4+} species was not observed. Mass gain was, however, observed on heating in CO_2 for $x \geq 0.6$, which increased and was displaced to lower temperatures with increasing Pr content, Fig. 8.

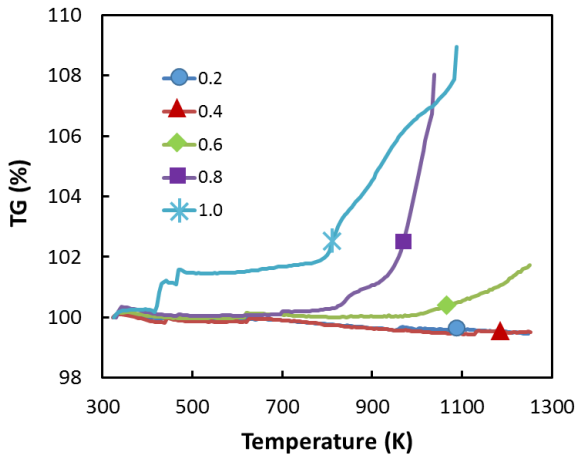

Fig. 8. TGA plots of the $Ba(Zr_{0.7}Ce_{0.2})_{1-x}Pr_xY_{0.1}O_{3-\delta}$ series in 100 % CO_2 with a heating rate of 5 $K.min^{-1}$.

Significant weight gain commenced at ~ 423 K for the x = 1.0 sample, reflecting the poor stability of this phase. The results are concurrent with the related $Ba(Zr_{0.7}Ce_{0.2})_{1-(x/0.9)}Pr_xY_{0.1}O_{3-\delta}$ series[15] and other Pr-doped $BaZrO_3$-based systems[12,41]. In our previous paper of the Ba stoichiometric series[15], we attributed the poorer stability of the Pr-doped samples to the larger average B-site cation radius forming a bond in which O is a better electron donor, and to a lower Goldschmidt tolerance factor, generally associated with poorer phase stability[42]. Notably, lowering the Ba chemical potential with respect to the Ba stoichiometric series does not have a positive effect on the phase stability in the present series.

Electrical conductivity

Impedance spectra obtained at 573 K in wet and dry N_2 and at 1173 K in wet N_2 for the x = 0.8 composition are shown in Fig. 9.

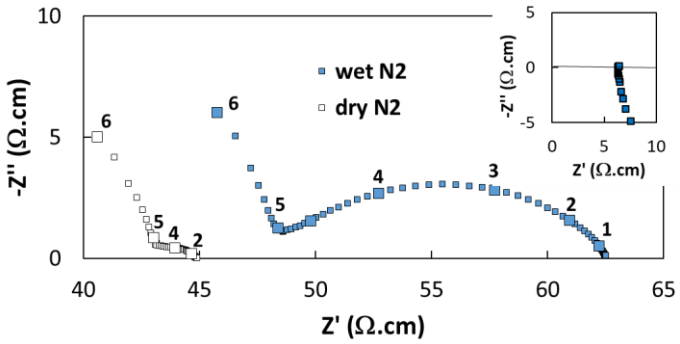

Fig. 9. Impedance spectra at 573 K in wet and dry N_2, and at 1173 K in N_2 (inset) for the x = 0.8 composition of the $Ba(Zr_{0.7}Ce_{0.2})_{1-x}Pr_xY_{0.1}O_{3-\delta}$ series; numbers refer to $\log_{10}$ of the frequency.

At high temperature, spectra were characterised by a purely resistive process attributable to the total resistance (inset, Fig. 9) in series with an autoinductive feature arising from the experimental set-up, with members of lower Pr content frequently presenting a small, additional electrode response. On decreasing temperature, at least two impedance contributions could generally be identified. Figure. 8 illustrates a typical response with a high-frequency feature of associated capacitance ~ 1×10^{-9} F indicative of a grain-boundary process[43], and a low-frequency pseudo semicircle with calculated capacitance of approximately 1×10^{-4} F, attributable to electrode-interface processes.

The temperature dependence of total conductivity of the $Ba(Ce_{0.2}Zr_{0.7})_{1-x}Pr_xY_{0.1}O_{3-\delta}$ series was determined from the impedance plots and is shown in dry air and N_2 in Fig. 10 (a) and (b), respectively, with comparisons of the conductivities in the two atmospheres for selected series members shown in Fig. 10 ((d)-(f)); corresponding activation energies are listed in Table 3.

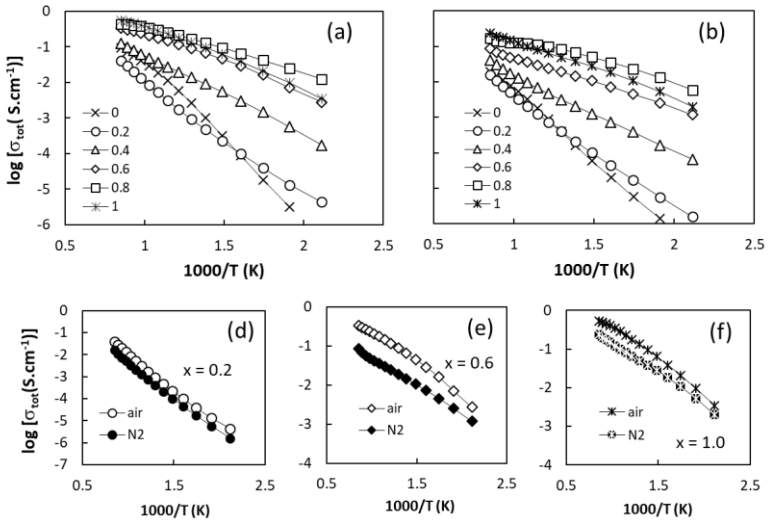

Fig. 10. Arrhenius plots of total conductivity for the $Ba(Zr_{0.7}Ce_{0.2})_{1-x}Pr_xY_{0.1}O_{3-\delta}$ series in (a) dry air, (b) dry N_2 and comparisons of conductivities in dry air and N_2 for selected compositions ((d)-(f)).

Conductivity is raised in the low-temperature range by around 4 orders of magnitude for the later series members in comparison to BZCY72 with a concomitant decrease in activation energy in all measured atmospheres. The activation energy in dry air decreases from 1 eV for the BZCY72 phase to 0.32 eV in the series member x = 0.8; however, the Pr-rich end member (x = 1) shows slightly higher activation energies and lower conductivity than the x = 0.8 sample, except for the highest measured temperatures in both dry air and N_2. Similar increases in conductivity with increasing Pr content are observed in the Ba stoichiometric series, and related $BaZrO_3$-based systems

on substituting with Pr [12,16]. We recently reported transport numbers for the Pr-free BZCY72 phase [3], which map the mixed ionic-electronic nature of conductivity in dry air and N_2. The higher conductivity in dry air in comparison to dry N_2 observed for the present series (Fig. 10) is also consistent with a significant p-type electronic contribution to transport, reflected in the lower activation energies with increasing x (Table 4). We note that the difference between conductivity in the two dry atmospheres is greater for later series members at high temperature, suggesting a greater role of electronic transport carriers at the expense of ionic species. As also observed in the previously studied $Ba(Zr_{0.7}Ce_{0.2})_{1-(x/0.9)}Pr_xY_{0.1}O_{3-\delta}$ system[15], the conductivities in dry air and N_2 become closer at low temperature, suggesting that this is a common feature of such perovskites. The trend towards convergence in the BZCY72 end member and Pr-lean phases in the two atmospheres at low temperature may be attributable to the higher activation energy of electron-hole conductivity with respect to oxide-ion conductivity [44,45] such that the ionic contribution to conductivity is higher at low rather than high temperatures. This has the effect that the conductivity is less affected by the oxygen activity of different atmospheres at lower temperature. A further consideration relevant to the highly electronic Pr-rich members is the higher mobility and concentration of electron holes at high temperature. Whereas the introduction of Pr in the Ba stoichiometric series alone had the effect of reducing the oxygen-vacancy concentration, partitioning of B cations on the Ba site also has a clear effect of lowering the oxygen-vacancy concentration, as discussed earlier (Fig. 7). The enthalpy change for the oxidation reaction

$$V_o^{\cdot\cdot} + ½O_2 \rightarrow O_o^{\times} + 2h^{\cdot} \qquad (4)$$

determined semi-empirically for $BaPr_{0.9}Gd_{0.1}O_{3-\delta}$[46] indicates that, at low temperature, the formation of holes is more favourable than that of oxygen vacancies. Note that the authors obtained positive enthalpy changes for the reverse reaction which states that eq. (4) is exothermic. We may expect, therefore, that electron holes are the dominant charge balancing the acceptor dopant:

$$[Y'_{Zr}] \approx [h^{\cdot}] \qquad (5)$$

The concentration of holes is, thus, fairly constant and mainly determined by the dopant content in the low-temperature range, such that changes in oxygen partial pressure have little effect on the concentration of charge carriers. As temperature increases, however, the formation of oxygen vacancies is more favourable (eq.(4) is displaced to the left) and they participate in maintaining electroneutrality (protons are considered negligible species in dry conditions):

$$[Y'_{Zr}] = 2[v_o^{\cdot\cdot}] + [h^{\cdot}] \qquad (6)$$

At high temperature, the creation of oxygen vacancies becomes the principal charge-compensation mechanism for the acceptor dopant. Concomitantly, the electronic conductivity approximates a classical +¼ power-law dependency , $\sigma_e \propto \log pO_2^{+1/4}$ [47]

where the difference in conductivities in dry air and dry N_2 is much more marked than at low temperature.

The oxidation states as determined from magnetic measurements and Rietveld refinement of neutron data (Fig. 7) indicate that Pr on the B site is likely to be present almost exclusively in the IV oxidation state. The origin of the electronic conductivity in this and the Ba stoichiometric series [15] may be considered, therefore, as holes residing in the oxygen band, since mixed Pr valence states on the perovskite B site may be discounted as the origin of the electronic hopping. Accordingly, the source of electronic conductivity of $BaPrO_3$ in oxidising conditions has been modelled as O^- species [48]. A similar situation arises in the current Ba-deficient system because, although the partitioning mechanism produces Pr^{3+} (Eq. 2), it is hosted in the A position of the perovskite, preventing the hopping of holes between different Pr species.

Arrhenius plots in wet and dry air and N_2 for selected samples are shown in Fig. 11.

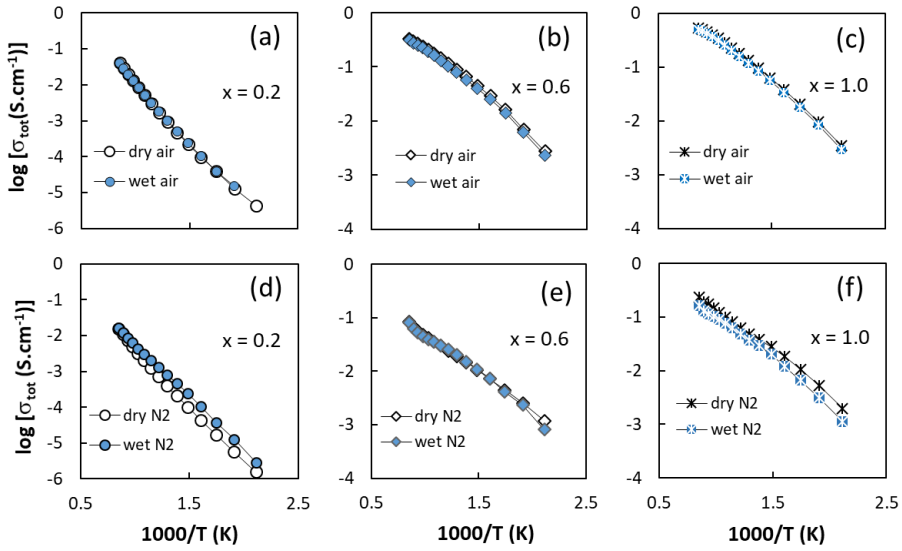

Fig. 11. Comparisons of temperature dependencies of total conductivity for selected members of the $Ba(Zr_{0.7}Ce_{0.2})_{1-x}Pr_xY_{0.1}O_{3-\delta}$ series in dry and wet air ((a)-(c)), and dry and wet N_2 ((d)-(f)).

The difference in conductivity between wet and dry air is marginal for the x = 0.2 sample (Fig.11 (a)), due to the dominating character of the electron-hole component at such high oxygen activities. Analogous to the Ba stoichiometric system, with increasing Pr content, increasingly lower conductivity values are observed in wet air in comparison to dry (Fig. 11(b) and (c)), consistent with the partial consumption of the dominating electron-hole species by less mobile protons according to the following defect reaction:

$$\frac{1}{2}H_2O + h^{\cdot} + O_O^{\times} \Leftrightarrow OH_O^{\cdot} + \frac{1}{2}O_2 \qquad (7)$$

The effect of lowering pO_2 in wet conditions for the Pr lean x = 0.2 sample (Fig. 11(a) and (d)) is to lower the electron-hole concentration (eq. (4)) such that the oxygen-vacancy content and, in turn, the proton content is significantly higher in the wet in comparison to dry atmosphere. In contrast, comparison of the Pr-rich phases in wet and dry N_2 (Fig.11 (e) and (f)) indicates a similar behaviour to that observed in air (Fig. 11 (b) and (c)), with electron-holes predominating transport irrespective of water content.

Conclusions

The technologically relevant BZCY72-$BaPrO_3$ system exhibits a wide interval of Ba substoichiometry, with a complete solid solution forming in the range $Ba(Zr_{0.7}Ce_{0.2})_{1-x}Pr_xY_{0.1}O_{3-\delta}$ ($0 \leq x \leq 1$) with various distortions of the perovskite structure. Symmetry changes in the sequence *Pnma* $\rightarrow$ *Imma* $\rightarrow R\bar{3}c \rightarrow Pm\bar{3}m$ were determined by Rietveld

refinement of neutron diffraction and synchrotron radiation X-ray diffraction, with greater octahedral tilting observed for higher Pr content and lower temperature in accordance with lowering of the tolerance factor. The refinements and magnetic-susceptibility data indicate that Ba substoichiometry is compensated by partitioning of multiple B-site cations on the perovskite A site with concomitant increase in the oxygen content. The lower tolerance factor with greater Pr content and more ionic B-O bonds are likely to cause the poor stability of Pr-rich phases in CO_2.

Pr substitution substantially increases electrical conductivity *via* electron-hole formation, as indicated by high refined oxygen contents for all series members and displacement of the temperature of oxygen loss to higher values with increasing Pr content. However, for lower Pr contents, as for the BZCY72 end member, oxygen-vacancy formation is competitive with hole formation such that protons contribute significantly to transport in wet, more reducing atmospheres.

Acknowledgements

We thank the MINECO, Spain (ENE2015-66183-R and MAT2016-78362-C4-1-R), CSIC, Spain (i-link0743) and CAPES, Brazil (PVE, Proceso 88881.03418/2013-1). Access to the neutron facilities at the Institut Laue Langevin (Grenoble, France) and the National Synchrotron Light Laboratory (LNLS, Campinas, Brazil) under grant 5-24-55(D2B) and research proposal D10B-XRD1-16166, respectively, is gratefully acknowledged. We also thank the FCT, PTDC/CTM-EME/6319/2014, QREN, FEDER and COMPETE Portugal and the European Social Fund, European Union. U A. acknowledges the Universidad San Pablo for financial support. We would also like to thank Steven Kermorvant and Alexandre Bosser of the IUT, University of Rennes (France) for assistance.

Table 1. Phase compositions and possible compensation mechanisms in the $Ba(Zr_{0.7}Ce_{0.2})_{1-x}Pr_xY_{0.1}O_{3-\delta}$ series.

x	nominal composition	vacancy mechanism	Pr partition mechanism	multiple cation partition mechansim
0	$BaZr_{0.7}Ce_{0.2}Y_{0.1}O_{3-\delta}$	-	-	
0.2	$Ba(Ce_{0.16}Zr_{0.56}Pr_{0.2}Y_{0.1})O_{3-\delta}$	$Ba_{0.980}(Zr_{0.549}Ce_{0.157}Pr_{0.196}Y_{0.098})O_{3-\delta}$	$(Ba_{0.990}Pr_{0.010})(Zr_{0.554}Ce_{0.158}Pr_{0.188}Y_{0.099})O_{3-\delta}$	$(Ba_{0.990}Pr_{0.002}Y_{0.008})(Zr_{0.554}Ce_{0.158}Pr_{0.196}Y_{0.091})O_{3-\delta}$
0.4	$Ba(Ce_{0.12}Zr_{0.42}Pr_{0.4}Y_{0.1})O_{3-\delta}$	$Ba_{0.962}(Zr_{0.404}Ce_{0.115}Pr_{0.385}Y_{0.096})O_{3-\delta}$	$(Ba_{0.980}Pr_{0.020})(Zr_{0.412}Ce_{0.118}Pr_{0.373}Y_{0.098})O_{3-\delta}$	$(Ba_{0.980}Y_{0.020})(Zr_{0.412}Ce_{0.118}Pr_{0.395}Y_{0.078})O_{3-\delta}$
0.6	$Ba(Ce_{0.08}Zr_{0.28}Pr_{0.6}Y_{0.1})O_{3-\delta}$	$Ba_{0.943}(Zr_{0.264}Ce_{0.075}Pr_{0.566}Y_{0.094})O_{3-\delta}$	$(Ba_{0.971}Pr_{0.029})(Zr_{0272}Ce_{0.078}Pr_{0.553}Y_{0.097})O_{3-\delta}$	$(Ba_{0.971}Pr_{0.006}Y_{0.023})(Zr_{0.272}Ce_{0.078}Pr_{0.576}Y_{0.074})O_{3-\delta}$
0.8	$Ba(Ce_{0.04}Zr_{0.14}Pr_{0.8}Y_{0.1})O_{3-\delta}$	$Ba_{0.926}(Zr_{0.130}Ce_{0.037}Pr_{0.741}Y_{0.093})O_{3-\delta}$	$(Ba_{0.962}Pr_{0.038})(Zr_{0.135}Ce_{0.038}Pr_{0.731}Y_{0.096})O_{3-\delta}$	$(Ba_{0.962}Pr_{0.023}Y_{0.015})(Zr_{0.135}Ce_{0.038}Pr_{0.746}Y_{0.081})O_{3-\delta}$
1.0	$Ba(PrY_{0.1})O_{3-\delta}$	$Ba_{0.909}(Pr_{0.909}Y_{0.091})O_{3-\delta}$	$(Ba_{0.952}Pr_{0.048})(Pr_{0.905}Y_{0.095})O_{3-\delta}$	$(Ba_{0.952}Pr_{0.031}Y_{0.017})(Pr_{0.922}Y_{0.078})O_{3-\delta}$

Table 2. Structural parameters, interatomic distances and agreement factors for selected members of the $Ba(Zr_{0.7}Ce_{0.2})_{1-x}Pr_xY_{0.1}O_{3-\delta}$ solid-solution series obtained from NPD data.

	***0.2* ($R\bar{3}c$)[a,c]**	***0.4* ($R\bar{3}c$)[a,d]**	***0.6* ($R\bar{3}c$)[a,e]**	***0.8* (*Imma*)[b,f]**
***a* (Å)**	6.0529(4)	6.0913(2)	6.1264(2)	6.1425(2)
***b* (Å)**	6.0529(4)	6.0913(2)	6.1264(2)	8.6684(2)
***c* (Å)**	14.802(2)	14.8588(9)	14.9327(7)	6.1790(2)
***V*(Å³)**	469.64(7)	477.45(4)	485.38(3)	329.01(2)
***A* position[g]**	6a	6a	6a	4e
z	-	-	-	0.0017(6)
***U_{iso}*×100 (Å²)**	1.10(4)	1.17(5)	1.14(4)	1.03(4)
***B* position[g]**	6b	6b	6b	4b
***U_{iso}*×100 (Å²)**	0.72(4)	0.64(4)	0.55(4)	0.65(3)
***O(1)* position**	18e	18e	18e	4e
x	0.4673(3)	0.4578(2)	0.4527(2)	-
z	-	-	-	-0.0649(4)
Occ	2.97(2)	3.02(2)	2.97(2)	0.97(1)
***U_{iso}*×100 (Å²)**	2.3(1)	2.3(1)	2.3(1)	1.8(1)
***O(2)* position**	-	-	-	8g
y	-	-	-	-0.0338(2)
Occ	-	-	-	2.07(2)
***U_{iso}*×100 (Å²)**	-	-	-	2.7(1)
Selected distances (Å)				
Ba-O(1)	3.224(1) × 3	3.298(1) × 3	3.3530(8) × 3	3.0987(6) × 2
	2.793(1) × 3	2.793(1) × 3	2.7734(8) × 3	2.699(4)
	3.048(1) × 6	3.048(1) × 6	3.0669(9) × 6	3.480(4)
Ba-O(2)	-	-		3.291(2) × 4
	-	-		2.868(2) × 4
Average Ba-O	3.073(1)	3.092(1)	3.0644(8)	3.084(2)
B-O(1)	2.1480(9) × 6	2.1654(9) × 6	2.1818(6) × 6	2.2039(5) × 2
B-O(2)				2.1978(2) × 4
Average B-O	2.1480(9)	2.1654(9)	2.1818(6)	2.1998(3)
***t-factor*[h]**	1.0116	1.0097	0.9932	0.9913

[a] Space Group $R\bar{3}c$, (# 62): 6a (0 0 ¼), 6b (0 0 0), 18e (x 0 ¼)

[b] Space Group *Imma*, (# 74): 4b (0 ½ ½), 4e (0 ¼ z), 8g (¼ y 0)

[c] T = 40 °C; χ^2= 1.26, R_{exp} = 3.59%, R_{wp}= 4.02 %, R_B = 1.42 %, $\rho_{(cryst)}$: 6.220 (1) g/cm³

[d] T = 26 °C; χ^2= 1.22, R_{exp} = 3.48 %, R_{wp}= 3.83 %, R_B = 1.62%, $\rho_{(cryst)}$: 6.291 (1) g/cm³

[e] T= 60 °C; χ^2= 1.42, R_{exp} = 4.05 %, R_{wp}= 4.82 %, R_B = 1.91%, $\rho_{(cryst)}$: 6.461(1) g/cm³

[f] T= 65 °C; χ^2= 1.23, R_{exp} = 4.07 %, R_{wp}= 4.52 %, R_B = 2.11%, $\rho_{(cryst)}$: 6.463 (1) g/cm³

[g] A and B cation occupancies are those of the multiple-cation partition mechanism, Table 1.

[h] Goldschmidt tolerance factor t = $\frac{d(A-O)}{\sqrt{2}\,d(B-O)}$

Table 3. Activation energy (in eV) of electrical conductivity for the $Ba(Zr_{0.7}Ce_{0.2})_{1-x}Pr_xY_{0.1}O_{3-\delta}$ as a function of Pr concentration, in dry and humidified air and N_2 atmospheres in the temperature range 523 – 723 K.

	dry		wet	
x	**air**	**N_2**	**air**	**N_2**
0	1.0	0.84	0.74	0.69
0.2	0.65	0.65	0.64	0.64
0.4	0.50	0.46	0.52	0.47
0.6	0.41	0.34	0.41	0.36
0.8	0.32	0.31	0.34	0.32
1	0.42	0.37	0.43	0.41

References

(1) Robinson, S.; Manerbino, A.; Grover Coors, W.; Sullivan, N. P. Fabrication and Performance of Tubular, Electrode-Supported $BaCe_{0.2}Zr_{0.7}Y_{0.1}O_{3-\delta}$ Fuel Cells. *Fuel Cells* **2013**, *13* (4), 584–591 DOI: 10.1002/fuce.201200191.

(2) Vasileiou, E.; Kyriakou, V.; Garagounis, I.; Vourros, A.; Stoukides, M. Ammonia Synthesis at Atmospheric Pressure in a $BaCe_{0.2}Zr_{0.7}Y_{0.1}O_{2.9}$ Solid Electrolyte Cell. *Solid State Ionics* **2015**, *275*, 110–116 DOI: 10.1016/j.ssi.2015.01.002.

(3) Heras-Juaristi, G.; Pérez-Coll, D.; Mather, G. C. Temperature Dependence of Partial Conductivities of the $BaZr_{0.7}Ce_{0.2}Y_{0.1}O_{3-\delta}$ Proton Conductor. *J. Power Sources* **2017**, *364*, 52–60 DOI: 10.1016/j.jpowsour.2017.08.011.

(4) Fabbri, E.; Markus, I.; Bi, L.; Pergolesi, D.; Traversa, E. Tailoring Mixed Proton-Electronic Conductivity of $BaZrO_3$ by Y and Pr Co-Doping for Cathode Application in Protonic SOFCs. *Solid State Ionics* **2011**, *202* (1), 30–35 DOI: 10.1016/j.ssi.2011.08.019.

(5) Duan, C.; Tong, J.; Shang, M.; Nikodemski, S.; Sanders, M.; Ricote, S.; Almansoori, A.; OHayre, R. Readily Processed Protonic Ceramic Fuel Cells with High Performance at Low Temperatures. *Science* **2015**, *349* (6254), 1321–1326 DOI: 10.1126/science.aab3987.

(6) Duan, C.; Hook, D.; Chen, Y.; Tong, J.; O'Hayre, R. Zr and Y Co-Doped Perovskite as a Stable, High Performance Cathode for Solid Oxide Fuel Cells Operating below 500 °C. *Energy Environ. Sci.* **2017**, *10* (1), 176–182 DOI: 10.1039/C6EE01915C.

(7) Xie, K.; Zhang, Y.; Meng, G.; Irvine, J. T. S. Electrochemical Reduction of CO_2 in a Proton Conducting Solid Oxide Electrolyser. *J. Mater. Chem.* **2011**, *21* (1), 195 DOI: 10.1039/c0jm02205e.

(8) Morejudo, S. H.; Zanon, R.; Escolastico, S.; Yuste-Tirados, I.; Malerod-Fjeld, H.; Vestre, P. K.; Coors, W. G.; Martinez, A.; Norby, T.; Serra, J. M.; Kjolseth, C. Direct Conversion of Methane to Aromatics in a Catalytic Co-Ionic Membrane Reactor. *Science* **2016**, *353* (6299), 563–566 DOI: 10.1126/science.aag0274.

(9) Antunes, I.; Mikhalev, S.; Mather, G. C.; Kharton, V. V.; Figueiras, F. G.; Alves, A.; Rodrigues, J.; Correia, M. R.; Frade, J. R.; Fagg, D. P. Site Redistribution, Partial Frozen-in Defect Chemistry, and Electrical Properties of $Ba_{1-x}(Zr,Pr)O_{3-\delta}$. *Inorg. Chem.* **2016**, *55*, acs.inorgchem.6b01084 DOI: 10.1021/acs.inorgchem.6b01084.

(10) Fabbri, E.; Bi, L.; Tanaka, H.; Pergolesi, D.; Traversa, E. Chemically Stable Pr and y Co-Doped Barium Zirconate Electrolytes with High Proton Conductivity for Intermediate-Temperature Solid Oxide Fuel Cells. *Adv. Funct. Mater.* **2011**, *21* (1), 158–166 DOI: 10.1002/adfm.201001540.

(11) Wang, Z.; Liu, M.; Sun, W.; Ding, D.; Lü, Z.; Liu, M. A Mixed-Conducting $BaPr_{0.8}In_{0.2}O_{3-\delta}$ Cathode for Proton-Conducting Solid Oxide Fuel Cells. *Electrochem. commun.* **2013**, *27*, 19–21 DOI: 10.1016/j.elecom.2012.10.037.

(12) Magrasó, A.; Frontera, C.; Gunnæs, A. E.; Tarancón, A.; Marrero-López, D.; Norby, T.; Haugsrud, R. Structure, Chemical Stability and Mixed Proton-Electron Conductivity in $BaZr_{0.9-x}Pr_xGd_{0.1}O_{3-\delta}$ *J. Power Sources* **2011**, *196* (22), 9141–9147 DOI: 10.1016/j.jpowsour.2011.06.076.

(13) Magrasó, A.; Espiell, F.; Segarra, M.; Irvine, J. T. S. Chemical and Electrical

Properties of $BaPr_{0.7}Gd_{0.3}O_{3-\delta}$. *J. Power Sources* **2007**, *169* (1), 53–58 DOI: 10.1016/j.jpowsour.2007.01.041.

(14) Antunes, I.; Mather, G. C.; Frade, J. R.; Gracio, J.; Fagg, D. P. Stability of $Ba(Zr,Pr,Y)O_{3-\delta}$ Materials for Potential Application in Electrochemical Devices. *J. Solid State Chem.* **2010**, *183* (12), 2826–2834 DOI: 10.1016/j.jssc.2010.09.021.

(15) Heras-Juaristi, G.; Amador, U.; Fuentes, R. O.; Chinelatto, A. L.; Romero De Paz, J.; Ritter, C.; Fagg, D. P.; Pérez-Coll, D.; Mather, G. C. Thermal Evolution of Structures and Conductivity of Pr-Substituted $BaZr_{0.7}Ce_{0.2}Y_{0.1}O_{3-\delta}$: Potential Cathode Components for Protonic Ceramic Fuel Cells. *J. Mater. Chem. A* **2018**, *6* (13), 5324–5334 DOI: 10.1039/c7ta09570h.

(16) Antunes, I.; Amador, U.; Alves, A.; Correia, M. R.; Ritter, C.; Frade, J. R.; Pérez-Coll, D.; Mather, G. C.; Fagg, D. P. Structure and Electrical-Transport Relations in $Ba(Zr,Pr)O_{3-\delta}$ Perovskites. *Inorg. Chem.* **2017**, *56* (15), 9120–9131 DOI: 10.1021/acs.inorgchem.7b01128.

(17) Slater, P. R.; Fagg, D. P.; Irvine, J. T. S. Synthesis and Electrical Characterisation of Doped Perovskite Titanates as Potential Anode Materials for Solid Oxide Fuel Cells. *J. Mater. Chem.* **1997**, *7* (12), 2495–2498 DOI: 10.1039/a702865b.

(18) Sun, Y.; Li, J.; Zeng, Y.; Amirkhiz, B. S.; Wang, M.; Behnamian, Y.; Luo, J. A-Site Deficient Perovskite: The Parent for in Situ Exsolution of Highly Active, Regenerable Nano-Particles as SOFC Anodes. *J. Mater. Chem. A* **2015**, *3* (20), 11048–11056 DOI: 10.1039/C5TA01733E.

(19) Azough, F.; Jackson, S. S.; Ekren, D.; Freer, R.; Molinari, M.; Yeandel, S. R.; Panchmatia, P. M.; Parker, S. C.; Maldonado, D. H.; Kepaptsoglou, D. M.;

Ramasse, Q. M. Concurrent La and A-Site Vacancy Doping Modulates the Thermoelectric Response of $SrTiO_3$: Experimental and Computational Evidence. *ACS Appl. Mater. Interfaces* **2017**, *9* (48), 41988–42000 DOI: 10.1021/acsami.7b14231.

(20) Mather, G. C.; García-Martín, S.; Benne, D.; Ritter, C.; Amador, U. A-Site-Cation Deficiency in the $SrCe_{0.9}Yb_{0.1}O_{3-\delta}$ Perovskite: Effects of Charge-Compensation Mechanism on Structure and Proton Conductivity. *J. Mater. Chem.* **2011**, *21* (15), 5764–5773 DOI: 10.1039/c0jm04464d.

(21) Yamazaki, Y.; Hernandez-Sanchez, R.; Haile, S. M. Cation Non-Stoichiometry in Yttrium-Doped Barium Zirconate: Phase Behavior, Microstructure, and Proton Conductivity. *J. Mater. Chem.* **2010**, *20* (37), 8158 DOI: 10.1039/c0jm02013c.

(22) Kim, H. S.; Bae, H. Bin; Jung, W. C.; Chung, S. Y. Manipulation of Nanoscale Intergranular Phases for High Proton Conduction and Decomposition Tolerance in $BaCeO_3$ Polycrystals. *Nano Lett.* **2018**, *18* (2), 1110–1117 DOI: 10.1021/acs.nanolett.7b04655.

(23) Rodriguez-Carvajal, J. Recent Advances in Magnetic Structure Determination by Neutron Powder Diffraction. *Phys. B* **1993**, *192*, 55–69.

(24) Mather, G. C.; Heras-Juaristi, G.; Ritter, C.; Fuentes, R. O.; Chinelatto, A. L.; Pérez-Coll, D.; Amador, U. A Structural Investigation of the BZCY72 Proton Conducting Oxide: Phase Transitions, Chemical Expansion and Deuteron Site. *J. Mater. Chem. A* **2016**.

(25) Glazer, A. M. Simple Ways of Determining Perovskite Structures. *Acta Crystallogr. Sect. A* **1975**, *31* (6), 756–762 DOI: 10.1107/S0567739475001635.

(26) Woodward, D. I.; Reaney, I. M. Electron Diffraction of Tilted Perovskites. *Acta Crystallogr. B.* **2005**, *61* (Pt 4), 387–399 DOI: 10.1107/S0108768105015521.

(27) Pérez-Coll, D.; Heras-Juaristi, G.; Fagg, D. P.; Mather, G. C. Transport-Number Determination of a Protonic Ceramic Electrolyte Membrane via Electrode-Polarisation Correction with the Gorelov Method. *J. Power Sources* **2014**, *245*, 445–455 DOI: 10.1016/j.jpowsour.2013.06.155.

(28) Hinatsu, Y. Magnetic Susceptibility and Electron Paramagnetic Resonance Spectrum of Tetravalent Praseodymium Ions in $BaPrO_3$. *J. Solid State Chem.* **1993**, *102*, 362–367.

(29) Hinatsu, Y.; Itoh, M.; Edelstein, N. Structure and Magnetic Properties of Tetravalent Praseodymium Perovskite SrPrO3. *J. Solid State Chem.* **1997**, *132* (2), 337–341 DOI: 10.1006/jssc.1997.7471.

(30) Bickel, M.; Goodman, G. L.; Soderholm, L.; Kanellakopoulos, B. The Magnetic Susceptibility of Pr^{4+} in $BaPrO_3$: Evidence of Long-Range Magnetic Order. *J. Solid State Chem.* **1988**, *76*, 178–185.

(31) Goossens, D. J.; Robinson, R. A.; Telling, M. T. F. The Antiferromagnetic Structure of $BaPrO_3$. *Phys. B Condens. Matter* **2004**, *352* (1–4), 105–110 DOI: 10.1016/j.physb.2004.06.061.

(32) Itoh, M.; Tezuka, K.; Wakeshima, M.; Hinatsu, Y. Magnetic Properties of $Ba_{1-x}La_xPrO_3$ and $PrLu_{1-y}Mg_yO_3$ with x and y <= 0.075. *J. Solid State Chem.* **1999**, *145* (1), 104–109 DOI: 10.1006/jssc.1999.8228.

(33) Itoh, M.; Hinatsu, Y. Crystal Structures and Magnetic Properties of $Ba_{1-y}Sr_yPrO_3$

(0≤ y ≤ 1.0). *J. Alloys Compd.* **1998**, *264*, 119–124.

(34) Hinatsu, Y. Magnetic Properties of Tetravalent Praseodymium Perovskites $BaPrO_3$, $BaCe_yPr_{1-y}O_3$, and $Sr_yBa_{1-y}PrO_3$. *J. Solid State Chem.* **1995**, *119* (2), 405–411 DOI: 10.1016/0022-4596(95)80059-X.

(35) D'Angelo, A. M.; Chaffee, A. L. Correlations between Oxygen Uptake and Vacancy Concentration in Pr-Doped CeO_2. *ACS Omega* **2017**, *2* (6), 2544–2551 DOI: 10.1021/acsomega.7b00550.

(36) Kruth, A.; Mather, G. C.; Jurado, J. R.; Irvine, J. T. S. Anomalous Variations of Unit Cell Parameters with Composition in Proton Conducting, $ACeO_3$-Type Perovskite Solid Solutions. *Solid State Ionics* **2005**, *176* (7–8), 703–712 DOI: 10.1016/j.ssi.2004.10.014.

(37) Howard, C. J.; Kennedy, B. J.; Chakoumakos, B. C. Neutron Powder Diffraction Study of Rhombohedral Rare-Earth Aluminates and the Rhombohedral to Cubic Phase Transition. *J. Phys. Condens. Matter* **2000**, *12* (4), 349–365 DOI: 10.1088/0953-8984/12/4/301.

(38) Hiraiwa, C.; Han, D.; Kuramitsu, A.; Kuwabara, A.; Takeuchi, H.; Majima, M.; Uda, T. Chemical Expansion and Change in Lattice Constant of Y-Doped $BaZrO_3$ by Hydration/Dehydration Reaction and Final Heat-Treating Temperature. *J. Amercian Ceram. Soc.* **2013**, *884* (31922), 879–884 DOI: 10.1111/jace.12172.

(39) Andersson, A. K. E.; Selbach, S. M.; Knee, C. S.; Grande, T. Chemical Expansion Due to Hydration of Proton-Conducting Perovskite Oxide Ceramics. *J. Am. Ceram. Soc.* **2014**, *2661*, 2654–2661 DOI: 10.1111/jace.12990.

(40) Mather, G. C.; Heras-Juaristi, G.; Ritter, C.; Fuentes, R. O.; Chinelatto, A. L.; Pérez-Coll, D.; Amador, U. Phase Transitions, Chemical Expansion and Deuteron Sites in the $BaZr_{0.7}Ce_{0.2}Y_{0.1}O_{3-\delta}$ Proton Conductor. *Chem. Mater.* **2016**, *28*, 4292–4299 DOI: 10.1021/acs.chemmater.6b01095.

(41) Magrasó, A.; Solans, X.; Irvine, J. T. S.; Segarra, M. Preparation of Stabilized Gd-Doped $BaPrO_3$ Materials by Zr Substitution. *Ceram. Int.* **2009**, *35* (5), 1819–1827 DOI: 10.1016/j.ceramint.2008.10.006.

(42) Yokokawa, H.; Kawada, T.; Dokiya, M. Thermodynamic Regularities in Perovskite and $K2NiF_4$ Compounds. *J. Am. Ceram. Soc.* **1989**, *72* (1), 152–153 DOI: 10.1111/j.1151-2916.1989.tb05971.x.

(43) Irvine, J. T. S.; Sinclair, D. C.; West, A. R. Electroceramics: Characterization by Impedance Spectroscopy. *Adv. Mater.* **1990**, *2* (3), 132–138 DOI: 10.1002/adma.19900020304.

(44) Song, S.-J.; Wachsman, E. D.; Dorris, S. E.; Balachandran, U. Electrical Properties of P-Type Electronic Defects in the Protonic Conductor $SrCe_{0.95}Eu_{0.05}O_{3-\delta}$. *J. Electrochem. Soc.* **2003**, *150* (6), A790 DOI: 10.1149/1.1574031.

(45) Sherafat, Z.; Paydar, M. H.; Antunes, I.; Nasani, N.; Brandão, A. D.; Fagg, D. P. Modeling of Electrical Conductivity in the Proton Conductor $Ba_{0.85}K_{0.15}ZrO_{3-\delta}$. *Electrochim. Acta* **2015**, *165*, 443–449 DOI: 10.1016/j.electacta.2015.03.018.

(46) Magrasó, A.; Haugsrud, R.; Segarra, M.; Norby, T. Defects and Transport in Gd-Doped $BaPrO_3$. *J. Electroceramics* **2008**, *23* (1), 80–88 DOI: 10.1007/s10832-008-9541-z.

(47) Ricote, S.; Bonanos, N.; Marco de Lucas, M. C.; Caboche, G. Structural and Conductivity Study of the Proton Conductor $BaCe_{(0.9-x)}Zr_xY_{0.1}O_{(3-\delta)}$ at Intermediate Temperatures. *J. Power Sources* **2009**, *193* (1), 189–193 DOI: 10.1016/j.jpowsour.2008.11.080.

(48) Stokes, S. J.; Islam, M. S. Defect Chemistry and Proton-Dopant Association in $BaZrO_3$ and $BaPrO_3$. *J. Mater. Chem.* **2010**, *20* (30), 6258–6264 DOI: 10.1039/c0jm00328j.